The Japan Society of Applied Physics

High-mobility transparent conductive thin films of cerium-doped hydrogenated indium oxide

View the article online for updates and enhancements.

High-mobility transparent conductive thin films of cerium-doped hydrogenated indium oxide

Eiji Kobayashi[1]*, Yoshimi Watabe[1], and Tetsuya Yamamoto[2]

[1]*Choshu Industry Co., Ltd., Sanyo Onoda, Yamaguchi 757-8511, Japan*
[2]*Kochi University of Technology, Kami, Kochi 782-8502, Japan*
E-mail: e.kobayashi@choshu.co.jp

We have developed 100-nm-thick cerium-doped hydrogenated indium oxide (ICO:H) films with a superior Hall mobility of 130–145 $cm^2 V^{-1} s^{-1}$. The ICO:H films deposited at 150 °C by dc arc-discharge ion plating were post-annealed at 200 °C. The relationship between the Hall mobility and carrier density of the polycrystalline ICO:H films shows that the carrier transport is limited by an ionized impurity scattering mechanism inside the grains. The surfaces of the ICO:H films were found to be very smooth and clear grain-boundary areas were not observed.
© 2015 The Japan Society of Applied Physics

A high carrier mobility of transparent conductive oxide (TCO) films in solar cells is required to coexist with the high optical transparency and low ohmic losses due to light absorption in the near-infrared (NIR) region, which is caused by plasma oscillations, in proportion to the free-carrier density.[1] Koida et al. showed that highly hydrogen-doped In_2O_3 (IO:H) exhibited a Hall mobility exceeding $100 \, cm^2 V^{-1} s^{-1}$.[2] Various dopants of metal species such as W,[3] Zr,[4] and Mo[5] have been used to dope polycrystalline In_2O_3 films to improve the crystallinity, thereby reducing intragranular lattice defects. We have been investigating the properties of Ce-doped[6] In_2O_3 films. That study was based on two factors with their corresponding effects: (i) the effective ionic radius of Ce^{4+} with a coordination number of 6 (0.101 nm)[7] is close to that of In^{3+} with the same coordination number (0.094 nm),[7] leading to the reduction of microstrain in the vicinity of the dopant sites; (ii) the density of the oxygen vacancies can be reduced by doped CeO_2 with a large standard formation enthalpy when compared to In_2O_3, resulting in crystallinity improvements. In this letter, we clarify the effects of both hydrogen doping with incorporated Ce and post-annealing on the structural and electrical properties of ICO:H films.

To this end, 100-nm-thick In_2O_3-based TCO films were deposited by dc arc-discharge ion plating (IP).[8] In_2O_3 with CeO_2 (ICO) contents of 3 wt % and pure In_2O_3 (IO) pellets (Sumitomo Metal Mining) were used as resource materials. The films were deposited on Corning Eagle XG glass substrates at 150 °C. The deposition gases were Ar, O_2 (8–13 vol %), and H_2 (0–2 vol %) and the total gas pressure during film deposition was 0.45 Pa. The ultimate vacuum pressure of the process chamber before the deposition was $\leq 1 \times 10^{-4}$ Pa. The film compositions were analyzed via rutherford backscattering spectrometry (RBS) and hydrogen forward scattering (HFS) using a CEA manufactured RBS system. The structural properties were analyzed by grazing incidence X-ray diffraction (XRD) scans using an MRS 6-axis diffractometer (PANalytical X'Pert Pro) equipped with a Cu X-ray tube and parallel-beam optics. The electric conductivity and Hall voltage were measured with a Hall effect measurement system (Toyo Technica ResiTest 8300). The grain size of the films was observed via field-emission scanning electron microscopy (FE-SEM; Hitachi High-Tech SU8240), while the surface morphology was characterized by atomic force microscopy (AFM; Park Systems, NX20).

Table I summarizes the In, Ce, O, and H compositions determined by RBS and HFS measurements for 100-nm-thick

Table I. In, Ce, O, and H compositions (in at. %) of ICO and ICO:H films subjected to post-annealing at 200 °C.

H_2/gas flow ratio (%)	In	Ce	O	H
0	34.0	0.7	64.6	0.7
1.0	35.7	0.6	62.4	1.3

ICO and ICO:H films deposited using H_2-gas with flow ratios of 0 and 1.0%, respectively, and identical oxygen partial pressures. The films were post-annealed at 200 °C for 30 min in air. Note that little difference in Ce compositions was observed between the two films, each being deposited by a different process. In addition, Table I shows that both ICO and ICO:H films show oxygen-richness in contrast with the stoichiometric composition of In_2O_3. As mentioned below, the XRD data analysis does not show segregation of Ce-oxides such as CeO_2 and Ce_2O_3 in those films. We confirmed the effect of Ce doping on the control of O composition in the films as described above; the density of the intragranular oxygen vacancies can be reduced. It is necessary to control the O composition in the films, taking into account the fact that oxygen interstitials with electron affinity would act as *n*-type killers within the grains and chemisorbed oxygen species at the grain boundaries with a negative charge (O^-) would form a barrier height to cause free-carrier scattering, resulting in the reduction of carrier mobility. Table I proves that co-doping of H with Ce donors with an increasing H_2-gas flow ratio leads to an increase in H composition together with a slight decrease in the atomic ratio of O species. This indicates that the O composition of the ICO matrix can be systematically controlled by changing the H_2-gas flow ratio with Ce doping content during the deposition, combined with the post-annealing step. This technique, which is based on co-doping mixed with post-annealing, can work very well, because it can enhance the carrier transport due to intra-granular microstructure improvements and it can reduce the contribution of grain-boundary scattering to the carrier transport. This will be discussed below.

Figure 1 shows grazing incidence XRD patterns of the ICO and ICO:H films with different H_2-gas flow ratios. All films were post-annealed at 200 °C for 30 min in air. The incidence angle was fixed at 1.0°. These data were plotted with a logarithmic intensity scale to overemphasize many weak peaks in the patterns. No peaks of Ce-oxides such as CeO_2 and Ce_2O_3 were observed. We investigated the effects
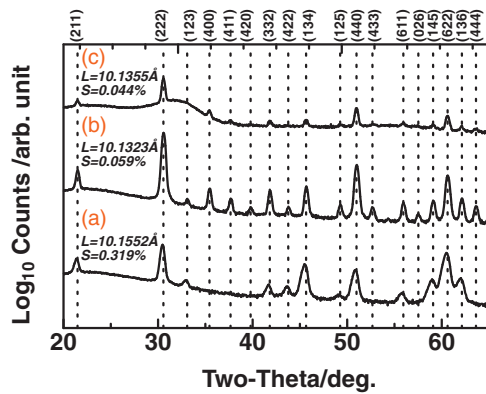
Fig. 1. Grazing incidence XRD profiles for (a) ICO, (b) ICO:H with a H_2-gas flow ratio of 1.0%, and (c) ICO:H with a H_2-gas flow ratio of 1.5%. All films were post-annealed at 200 °C for 30 min in air.

Fig. 2. Hall mobility versus carrier density for ICO, ICO:H, and IO:H films, which were all subjected to post-annealing at 200 °C for 30 min in air.

of post-annealing and H doping on the crystal microstructure, paying special attention to lattice parameters and residual strain.

Note that no peaks for as-deposited ICO:H films were observed. We found the effect of the post-annealing on the structure of the films. The amorphous phase of as-deposited ICO:H films changed to a bixbyte In_2O_3 polycrystalline structure: the angles of the diffracted peaks were almost identical to those of ITO containing 6.25% of Sn (dotted line).[9]

Firstly, lattice parameters (l) were estimated from the peaks that were identified for each film. Then, the lattice parameter (L) was defined as the average of all l-values. In addition, the residual strain (S) in each film was calculated on the basis of the size-strain analysis of the peak data obtained by the strain model. The L and S values obtained for each film are shown in Fig. 1. Herein, we found that H doping reduces both the L and S values of the ICO films.

Figure 2 shows the relationship between the Hall mobility (μ_H) and carrier density (N) for the post-annealed ICO and ICO:H films with H_2-gas flow ratios ranging from 1.0 to 2.0%. For comparison, the data for post-annealed IO:H with H_2-gas flow ratios in the range of 1.0 to 2.0% were added. Note that the Hall motility of the ICO:H films with a H_2-gas flow ratio of 1.0% shows higher values, given by 130–145 $cm^2 V^{-1} s^{-1}$, when compared to those corresponding to IO:H films.

The carrier mobility that is limited by ionized impurity scattering, μ_I, was calculated by the Brooks–Herring–Dingle (BHD) theory,[10,11] including both degeneracy and non-parabolicity of the conduction bands.[12] On the other hand, the carrier mobility that is limited by grain boundary scattering, μ_G, was calculated based on the Seto theory.[13] For increasing values of N of up to $\sim 1 \times 10^{20}$ cm^{-3}, μ_I is larger than μ_G. When N is further increased, μ_G becomes larger than μ_I. Note that the expression $\mu_H^{-1} = \mu_G^{-1} + \mu_I^{-1}$ cannot explain the values of μ_H for ICO:H films with a H_2-gas flow ratio of 1.0%. The experimental data and the expression above imply that μ_G is very large compared to μ_I. We thus concluded that ionized impurity scattering is a dominant factor that limits the carrier mobility in such films. Figure 2 shows that the expression above explains the behavior of μ_H for all other ICO:H films, including ICO:H films with H_2-gas flow ratios of 1.5 and 2.0%, and ICO films
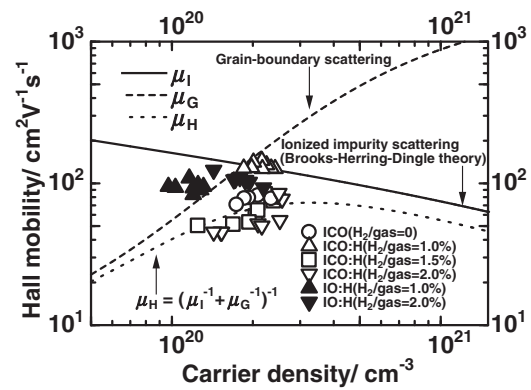
very well. It can be concluded that both ionized impurity scattering and grain boundary scattering determine the carrier mobility of those films. In addition, it should be mentioned that the two ICO:H films for which H_2-gas flow ratios of 1.5 and 2.0% were used exhibit a crystal-grown area and an amorphous area, as discussed below. In such films with mixed structures, the scattering mechanism in the amorphous area also contributes to the carrier transport in the films. On the other hand, for IO:H films, additional study is required.

Figure 3 shows the back scattered electron (BSE) images of the surface structures of ICO, ICO:H, and IO:H films captured by FE-SEM. The grains of the post-annealed ICO film were clearly observed for sizes of and below 100 nm, as shown in Fig. 3(a). The grain boundaries of the as-deposited ICO:H film with a H_2-gas flow ratio of 1.0% were not clearly observed [Fig. 3(b)]. Note that Figs. 3(c) and 3(d) show conspicuous grains with kaleidoscope patterns for the post-annealed ICO:H films. Figures 3(e) and 3(f) show both the crystal-grown and amorphous areas for post-annealed ICO:H films with a H_2-gas flow ratio of 1.5%, which is consistent with the results displayed by Fig. 1(c). The grains of the post-annealed IO:H film deposited with a H_2-gas flow ratio of 1.0% were observed to be over 1 µm in size [Fig. 3(g)], whereas the grains of the post-annealed IO:H film with a H_2-gas flow ratio of 2.0% were not clearly observed, similarly to those of the previously mentioned ICO:H films deposited with a H_2-gas flow ratio of 1.0%.
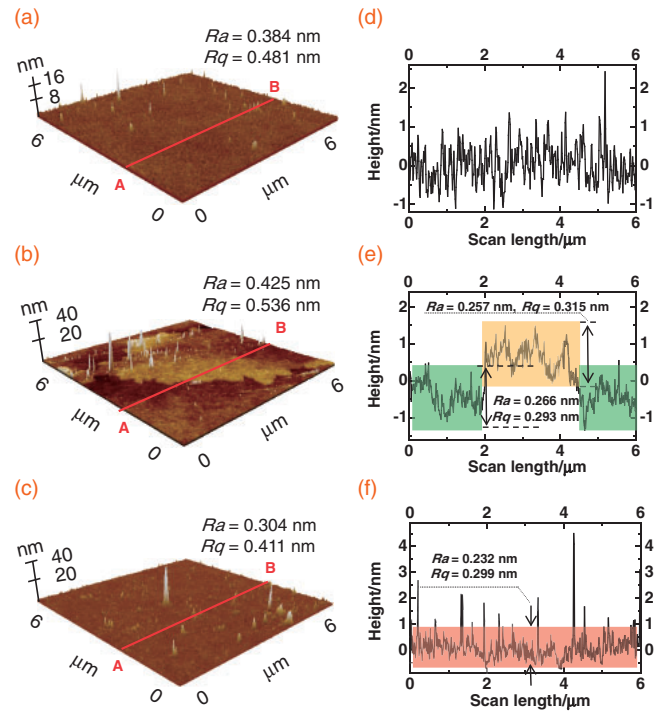
Figure 4 shows the AFM images of post-annealed ICO, next to those corresponding to as-deposited and post-annealed ICO:H with a H_2-gas flow ratio of 1.0%. The one-dimensional cross-sectional scans of surface profiles are added to Fig. 4. We assumed that signals measured within the field with a height of 2 nm or higher were particles generated when the glass substrates were scrubbed. The AFM results, which include the calculated average surface roughness (R_a) and root-mean-square roughness (R_q), show that the surface of the post-annealed ICO:H film was smoother than that of other films. Spiky signals with heights ranging from 1 to 2 nm were observed on the film surface. Note that the R_a value excluding these signals was just 0.232 nm [see Fig. 4(f)]. The spiky signals could not be identified from the analyzed data obtained by FE-SEM and AFM measurements, making it unclear whether they originate in the particles or due to projections from the film. On the other hand, island
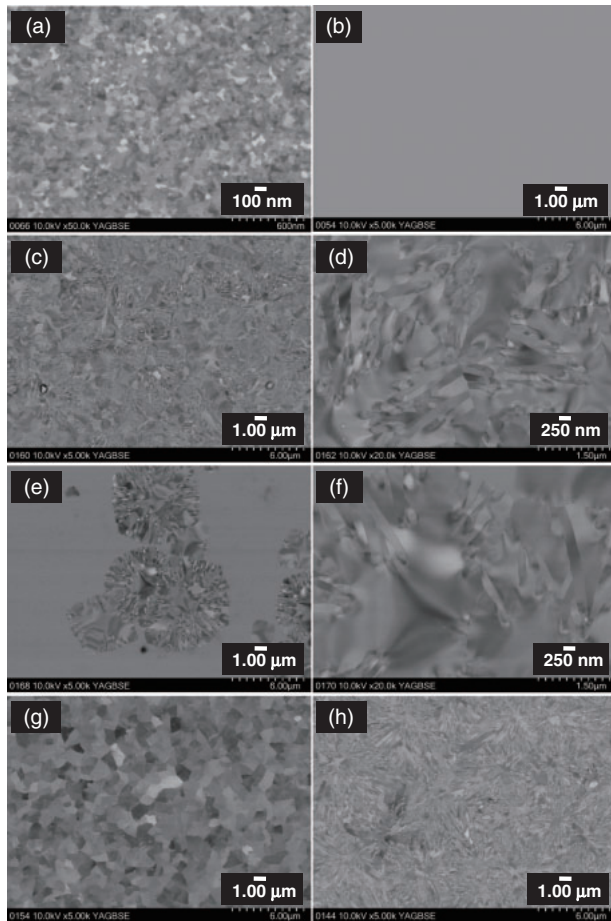
Fig. 3. BSE images of the surface morphologies of (a) post-annealed ICO, (b) as-deposited ICO:H with a H_2-gas flow ratio of 1.0%, (c, d) post-annealed ICO:H with a H_2-gas flow ratio of 1.0%, (e, f) post-annealed ICO:H with a H_2-gas flow ratio of 1.5%, (g) post-annealed IO:H with a H_2-gas flow ratio of 1.0%, and (h) post-annealed IO:H with a H_2-gas flow ratio of 2.0%. Post-annealing was performed at 200 °C for 30 min in air.

Fig. 4. AFM images of (a) post-annealed ICO, (b) as-deposited ICO:H with a H_2-gas flow ratio of 1.0%, (c) post-annealed ICO:H with a H_2-gas flow ratio of 1.0%, and (d)–(f) line scan profiles (A–B lines) corresponding to (a)–(c), respectively. The post-annealing was performed at 200 °C for 30 min in air. The average surface roughness (R_a) and root-mean-square roughness (R_q) are also shown.

structures with a height of 1 nm were observed on the surface of the as-deposited ICO:H film [see Fig. 4(b)]. The R_a values of internal and external island structures were 0.257 and 0.266 nm, respectively [see Fig. 4(e)]. Taking into account the fact that annealed films had smoother surfaces than as-deposited films, as shown by Figs. 4(b) and 4(c), we concluded that those island structures on the as-deposited ICO film disappeared after annealing: in this process, the atoms in the island structures moved inside the film during the recrystallization of the solid phase. The post-annealing technique employed in this work is a key to achieve ICO:H films that have a high Hall mobility together with smooth surfaces.

In these experiments, we obtained the following results. Post-annealed ICO:H films with a thickness of 100 nm deposited by ion plating at 150 °C show a superior Hall mobility of 130–145 $cm^2 V^{-1} s^{-1}$ and exhibit very smooth surfaces.

Analysis of the relationship between the Hall mobility and carrier density showed that the dominant factor that limits the carrier transport of the films is an intragranular ionized impurity scattering mechanism. These findings prove that these films have great potential for their application in solar cells.

1) I. Hamberg and C. G. Granqvist, J. Appl. Phys. **60**, R123 (1986).
2) T. Koida, H. Fujiwara, and M. Kondo, J. Non-Cryst. Solids **354**, 2805 (2008).
3) P. F. Newhouse, C.-H. Park, D. A. Keszler, J. Tatea, and P. S. Nyholm, Appl. Phys. Lett. **87**, 112108 (2005).
4) T. Koida and M. Kondo, J. Appl. Phys. **101**, 063705 (2007).
5) Y. Meng, X. Yang, H. Chen, J. Shen, Y. Jiang, Z. Zhang, and Z. Hua, Thin Solid Films **394**, 218 (2001).
6) N. Mori, J. Ueno, Y. Uesugi, and K. Miki, e-J. Surf. Sci. Nanotechnol. **10**, 471 (2012).
7) R. D. Shannon, Acta Crystallogr., Sect. A **32**, 751 (1976).
8) Y. Shigesato, S. Takaki, and T. Haranoh, J. Appl. Phys. **71**, 3356 (1992).
9) N. Nadaud, N. Lequeux, M. Nanot, J. Jove, and T. Roisnel, J. Solid State Chem. **135**, 140 (1998).
10) C. Erginsoy, Phys. Rev. **79**, 1013 (1950).
11) R. B. Dingle, Philos. Mag. **46**, 831 (1955).
12) T. Pisarkiewicz, K. Zakrzewska, and E. Leja, Thin Solid Films **174**, 217 (1989).
13) J. Y. W. Seto, J. Appl. Phys. **46**, 5247 (1975).